

Simultaneous Brillouin and piezoelectric coupling to a high-frequency bulk acoustic resonator

TAEKWAN YOON,^{1,2,†,*} DAVID MASON,^{1,2,†} VIJAY JAIN,^{1,2} YIWEN CHU,³ PRASHANTA KHAREL,^{1,2}  WILLIAM H. RENNINGER,⁴ LIAM COLLINS,⁵ LUIGI FRUNZIO,^{1,2} ROBERT J. SCHOELKOPF,^{1,2,6} AND PETER T. RAKICH^{1,2,7}

¹Department of Applied Physics and Physics, Yale University, New Haven, Connecticut 06520, USA

²Yale Quantum Institute, New Haven, Connecticut 06520, USA

³Department of Physics, ETH Zurich, 8093 Zurich, Switzerland

⁴Institute of Optics, University of Rochester, Rochester, New York 14627, USA

⁵Center for Nanophase Materials Sciences, Oak Ridge National Laboratory, Oak Ridge, Tennessee 37831, USA

⁶e-mail: robert.schoelkopf@yale.edu

⁷e-mail: peter.rakich@yale.edu

*Corresponding author: taekwan.yoon@yale.edu

Received 24 August 2022; revised 1 December 2022; accepted 2 December 2022; published 17 January 2023

Bulk acoustic resonators support robust, long-lived mechanical modes, capable of coupling to various quantum systems. In separate works, such devices have achieved strong coupling to both superconducting qubits, via piezoelectricity, and optical cavities, via Brillouin interactions. In this work, we present a hybrid microwave–optical platform capable of coupling to bulk acoustic waves through cavity-enhanced piezoelectric and photoelastic interactions. The modular, tunable system achieves fully resonant and well-mode-matched interactions among a 3D microwave cavity, a high-frequency bulk acoustic resonator, and a Fabry–Perot cavity. We realize this piezo–Brillouin interaction in x-cut quartz, demonstrating the potential for strong optomechanical interactions and high cooperativity using optical cavity enhancement. We further show how this device functions as a bidirectional electro–opto–mechanical transducer, with transduction efficiency exceeding 10^{-8} , and a feasible path towards unity conversion efficiency. The high optical sensitivity and ability to apply a large resonant microwave field in this system also offers a tool for probing anomalous electromechanical couplings, which we demonstrate by investigating (nominally centrosymmetric) CaF_2 and revealing a parasitic piezoelectricity of 83 am/V. Such studies are an important topic for emerging quantum technologies, and highlight the versatility of this hybrid platform. © 2023 Optica Publishing Group under the terms of the [Optica Open Access Publishing Agreement](#)

<https://doi.org/10.1364/OPTICA.474022>

1. INTRODUCTION

Acoustic resonators with long-lived modes have played an important technological role in systems ranging from ultrastable oscillators to micro–electro–mechanical devices. For quantum applications, acoustic devices offer the promise of flexibly linking disparate quantum systems through a wide variety of coupling pathways [1]. Mechanical resonators have achieved quantum-coherent coupling to systems ranging from optical and microwave cavities, to solid state defect centers, atomic ensembles, and superconducting qubits [2–8]. These advances relied on high-quality-factor (Q) mechanical resonators, building on phononic engineering and low material dissipation at cryogenic temperatures [9,10]. Among mechanical systems, high-overtone bulk acoustic resonators (HBARs), where high-frequency elastic standing waves are formed between polished surfaces of a crystalline substrate, offer a promising platform for achieving highly acoustic Q-factors [11]. By design, these modes live primarily in the bulk, avoiding the loss typically associated with surface imperfections. Moreover,

acoustic loss from phonon–phonon scattering plummets at cryogenic temperatures [11–13], offering an ideal environment for long-lived acoustic modes.

To achieve strong optical interactions with these acoustic modes, one can exploit phase-matched photoelastic coupling, known as Brillouin scattering [14–17]. This three-wave interaction can yield strong optomechanical coupling to GHz-frequency acoustic modes, particularly when the process is enhanced by an optical cavity. One can also couple microwave fields directly to the acoustic modes via resonant piezoelectric interaction. Using these interactions, in separate systems, bulk acoustic resonators have achieved strong coupling to both superconducting circuits and optical cavities [8,17–19].

Here, we present, for the first time, a system integrating simultaneous piezoelectric and Brillouin coupling to a GHz bulk acoustic resonator, in a hybrid system containing both a microwave and an optical cavity. To demonstrate the mechanism behind this

piezo-Brillouin interaction, we first present a single-pass configuration (i.e., without the benefit of optical cavity enhancement), using a microwave cavity to drive GHz phonon modes in x-cut quartz, and reading out scattered optical photons. We then incorporate an optical cavity to realize a fully resonant operation where both electromechanical and optomechanical coupling mechanisms are cavity enhanced, boosting interaction rates by orders of magnitude. The use of a modular Fabry-Perot cavity offers frequency tunability to meet this multiply resonant condition, while maintaining low-loss optical modes.

We observe strong optomechanical interactions (characterized by cooperativity exceeding unity), even reaching strong coupling. Along with competitive coupling efficiencies and robust thermal properties, this reveals the potential of this hybrid platform for microwave-optical transduction with quantum applications [20–34]. Realizing efficient quantum state conversion is of critical importance for optically linking superconducting quantum devices, and remains an outstanding goal for the field. Here, we present bidirectional conversion with transduction efficiency comparable to other developing piezo-optomechanical platforms [24–29,35], and we outline a feasible path for improvement.

We further demonstrate that the optical performance of this system offers a highly sensitive method for detecting piezoelectrically driven phonons, offering a new tool for materials analysis. We illustrate this by interrogating CaF_2 , revealing an anomalous piezoelectric coupling, which may indicate surface damage or lattice defects in the bulk [36–38]. Probing such effects in technologically relevant materials (e.g., sapphire or diamond) can offer clues to understanding loss mechanisms for quantum systems [39,40].

2. DEMONSTRATION OF SINGLE-PASS PIEZO-BRILLOUIN SPECTROSCOPY

Our hybrid platform [illustrated in Fig. 1(a)] is designed to achieve fully resonant microwave and optical coupling to an HBAR device. In contrast to integrated nanomechanical devices, this platform is an assembly of three distinct resonators (acoustic, optical, and microwave). This modular design enables independent optimization of each resonator, including Q-factors and mode matchings. The optical and microwave frequencies are individually tunable, to allow resonant coupling to virtually any transparent crystalline material. We demonstrate this hybrid piezo-Brillouin interaction using x-cut quartz—a piezoelectric material with good acoustic performance.

The platform design centers around the use of an HBAR that supports longitudinal elastic standing waves confined between the opposing surfaces of a crystalline substrate. At modest cryogenic temperatures ($T \sim 4$ K), these Fabry-Perot-like acoustic modes can achieve Q-factors at GHz (MHz) frequencies in excess of 10^7 (10^9), by working with high-purity crystals with smooth surfaces [11,41]. While plano-convex crystals offer stable resonances with the highest mechanical Q, here, we work with flat, unprocessed substrates for material flexibility and simplified assembly. Acoustic modes of a flat-flat resonator experience diffraction loss, but still reach $Q > 10^4$. The substrate hosts a set of longitudinal modes, spaced by a mechanical free spectral range (FSR), $\Delta_m = v_m/2L_m$, determined by the sound velocity, v_m , and substrate thickness, L_m . Here, we work with a 0.5 mm thick x-cut quartz substrate, with acoustic loss rate of $\Gamma/2\pi \approx 500$ kHz and $\Delta_m/2\pi \approx 5.5$ MHz.

For electromechanical coupling to the HBAR, we rely on resonant piezoelectric interactions with a microwave resonator as

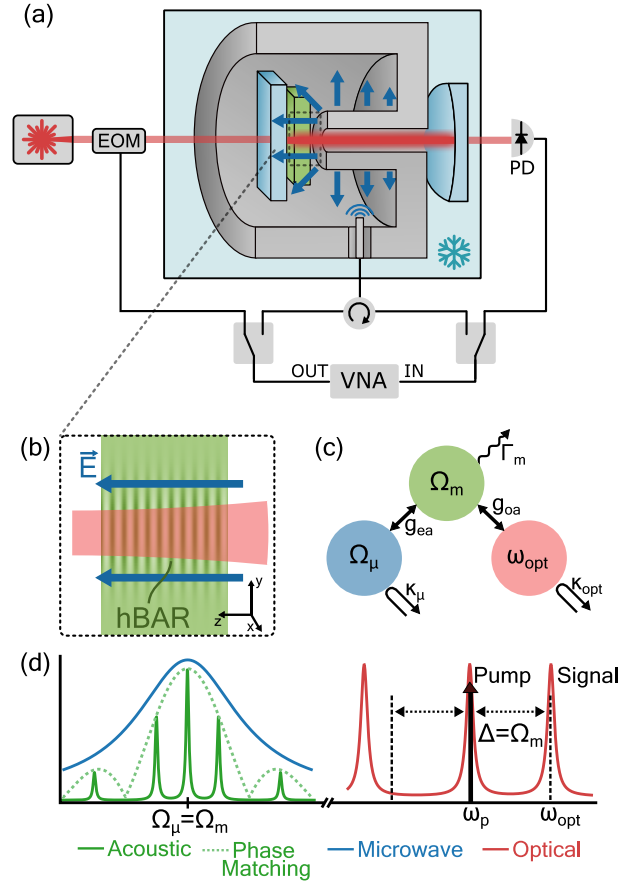


Fig. 1. Hybrid piezo-Brillouin optomechanical system. (a) Cross section of the hybrid cavity and simplified experimental schematic, showing the acoustic resonator (green), microwave cavity (gray), and optical mirrors (light blue). Dark blue arrows indicate microwave E-field, dark green indicates the longitudinal acoustic mode of the HBAR, and red denotes optical light. Microwave and optical signals can be injected by driving the microwave cavity or electro-optic modulator (EOM), respectively. Optical signals are detected in transmission (at photodiode, PD), using the pump light as a heterodyne local oscillator. Microwave signals can be collected and amplified directly from the cavity. Experiment conducted in He-4 flow cryostat, $T \approx 10$ K. See Supplement 1 for detailed experimental schematic. (b) Inset showing overlap among the microwave/optical/acoustic modes (c) Simplified illustration of mode couplings and decay pathways for the optical (red), microwave (blue), and acoustic (green) modes. (d) Spectral response of microwave (blue), optical (red), and acoustic (green) modes, including the Brillouin phase-matching bandwidth (dashed green). The Stokes and anti-Stokes sideband frequencies are indicated by black dashed lines, symmetrically spaced around the pump (ω_p , black arrow). Only the anti-Stokes is resonant with an optical mode (at ω_{opt}). Non-uniform optical mode spacing is caused by Fresnel reflections at the vacuum-dielectric interface of the crystal within the cavity [17].

shown in Fig. 1(c). We require a microwave resonator that can match the acoustic frequency (10–50 GHz), ideally with high Q-factor and easy tunability. A coaxial stub cavity [see Fig. 1(a)], a common resource for quantum technologies, is well suited for this task [42]. In such a resonator, the microwave field is concentrated around a quarter-wavelength central post, allowing for easy adjustment of the resonance frequency via the post length. The monolithic cavity geometry eliminates seam losses, which is beneficial in creating high-Q cavities. Combined with the use

of superconducting materials, the Q-factor of a coaxial stub cavity can exceed $Q_\mu > 10^7$ [42]. Here, we work at $T = 4$ K, and choose (non-superconducting) copper for its thermal conductivity and low electrical resistivity, reaching a microwave loss rate of $\kappa_\mu/2\pi \approx 17$ MHz, and corresponding internal Q-factor of $Q_\mu \approx 1200$. Additionally, we make a small (1 mm diameter) aperture through the stub to allow for optical access, which has a negligible impact on the Q-factor of the microwave design.

The coaxial microwave cavity is resonantly coupled, via the piezoelectric effect, to an HBAR located above the central post. Electromagnetic simulations [Ansys High Frequency Simulation Software (HFSS)] show that the electric field is oriented perpendicular [i.e., z direction; see Fig. 1(b)] to the substrate, and is approximately uniform across the substrate thickness. This field resonantly couples to the longitudinal acoustic mode via the d_{33} element of the piezoelectric tensor. Note that all crystal axis indices are assumed to be in the reference frame of the substrate. Specifically, the piezoelectric interaction is described by the coupling rate, $\hbar g_{\text{em}} = c_{33} d_{33} \int E_z S_{zz} dV$, where $S_{zz} = \frac{\partial U_z}{\partial z}$ is the longitudinal strain, expressed in terms of the z displacement, U_z , E_z is the z component of the microwave electric field, and c_{33} is the relevant stiffness coefficient. While the acoustic mode oscillates along the z axis with a sub-micrometer wavelength, the microwave electric field is uniform along the thickness of the crystal. As a consequence, the electromechanical mode-matching integral vanishes for acoustic modes with even longitudinal indices. Odd-indexed modes couple at a rate of

$$g_{\text{em}} = \frac{d_{33} E_0 \lambda_m}{\pi} \sqrt{\frac{\Omega_m c_{33} A_m}{2 \hbar L_m}}, \quad (1)$$

where E_0 is the zero-point field strength, λ_m (Ω_m) is the acoustic wavelength (frequency), A_m is the effective area of the acoustic mode, and L_m is the acoustic substrate thickness (see Supplement 1 for derivation). The interaction strength of the microwave and acoustic resonators can be characterized by the electromechanical cooperativity, $C_{\text{em}} = \frac{4g_{\text{em}}^2}{\kappa_\mu \Gamma}$. From these piezoelectricity and microwave simulations, we estimate the electromechanical coupling in this quartz system to be $g_{\text{em}}/2\pi = 298$ Hz, corresponding to $C_{\text{em}} = 4.18 \times 10^{-8}$. It is important to use cryogenic values for quartz piezoelectricity [43], as it can vary $\sim 50\%$ at cryogenic (5 K) temperatures.

Optomechanical coupling is realized through Brillouin scattering, which is a three-wave interaction between optical pump/signal fields and an acoustic wave, mediated by photoelasticity [14,15]. Brillouin scattering offers a distributed, phase-matched interaction that takes place throughout the bulk of the crystal. This is advantageous compared with conventional radiation pressure optomechanical coupling, which is relatively weak due to the large acoustic mode volume of HBARs. The Brillouin interaction is described by the single-photon coupling rate, $\hbar g_{\text{om},0} = \frac{1}{2} \epsilon_0 \epsilon_r p_{13} \int S_{zz} E_{\text{opt}}^2 dV$, where E_{opt} is the transverse electric field of the optical cavity (assumed to be along \hat{x} here), p_{13} is the relevant photoelastic coefficient, and ϵ_0 (ϵ_r) is the vacuum (relative material) permittivity [15,44]. The mode overlap is maximized when the modes satisfy a phase-matching condition, $2k_{\text{opt}} \cong q$, where k_{opt} (q) is the optical (acoustic) wave vector. This phase-matching condition implies that the acoustic wavelength should approximately match half of the optical wavelength in

the medium. This results in non-zero couplings to a small number of acoustic modes centered around the Brillouin frequency ($\Omega_B = 2\omega_p n v_m/c$), where ω_p is the optical pump frequency, n is the refractive index, and v_m is the acoustic velocity in the substrate. For x-cut quartz, the Brillouin frequency is $\Omega_m/2\pi \approx 11.4$ GHz for $\lambda_{\text{opt}} \approx 1550$ nm. Hereafter, we designate the longitudinal mode best satisfying this phase-matching condition as the primary mechanical mode of interest, with frequency Ω_m [see Fig. 1(d)]. For this phase-matched mode, the Brillouin optomechanical coupling rate is [15,17]

$$g_{\text{om},0} = \frac{\omega_p^2 n^3 p_{13}}{2c} \sqrt{\frac{\hbar}{\Omega_m \rho A_m L_m}}, \quad (2)$$

where ρ is the density, and c is the speed of light. Note that here we assumed that the acoustic mode area is defined by the optical mode area $A_{\text{opt}}/2 = A_m$ (see Supplement 1). Other acoustic modes are suppressed by a $\text{sinc}^2[(\Omega - \Omega_B)/4\Delta_m]$ envelope that originates from the phase-matching condition. Drawing an analogy to cavity-optomechanics [45], $g_{\text{om},0}$ can be linearized around a strong optical pump, resulting in an enhanced interaction between the acoustic mode and optical signal field. This enhanced coupling rate is given by $g_{\text{om}} = \sqrt{N} g_{\text{om},0}$, where N is the number of pump photons in the crystal.

Brillouin scattering measurements are conventionally implemented in a single-pass configuration, where a strong pump can interact with acoustic phonons, scattering into backwards-propagating Stokes and anti-Stokes fields. In this configuration, a Brillouin-active phonon mode, with population n_m , will scatter incident pump photons to an anti-Stokes sideband with power $P_{\text{sig}} = (\hbar \omega_p) C_{\text{om}}^{\text{sp}} \Gamma n_m$. Here, $C_{\text{om}}^{\text{sp}} = \frac{g_{\text{om}}^2}{\Gamma \tau - 1}$ is the single-pass equivalent of a cavity cooperativity [15], in terms of the group delay $\tau = L_m n/c$ (see Supplement 1). Figure 2(d) presents such a Brillouin signal, from piezoelectrically driven phonons, using the previously described microwave cavity and x-cut quartz HBAR. We sweep a 3.8 mW microwave drive over a ~ 40 MHz range around Ω_B while measuring the coherent backscattered optical signal, detected as a heterodyne beat note with reflected pump light. We see a series of acoustic resonances with $\Gamma/2\pi \approx 500$ kHz and the expected mode spacing $\Delta_m \approx 5.5$ MHz. The resonances away from Ω_B are suppressed according to the optical phase-matching condition and microwave cavity susceptibility. For this single-pass measurement, we theoretically estimate the single-photon coupling rate to be $g_{\text{om},0}/2\pi = 156$ Hz. For our pump power ($P = 67$ mW), this gives a field-enhanced $g_{\text{om}}/2\pi = 180$ kHz ($C_{\text{om}}^{\text{sp}} = 1.1 \times 10^{-6}$), which predicts the observed signal size within 5 dBm [see Fig. 2(d)]. The discrepancy can be attributed to the uncertainties in material constants at cryogenic temperatures. While this measurement demonstrates piezo-Brillouin interaction, it is desirable to have higher optomechanical coupling for broader applications, ideally exceeding a cooperativity of unity. To achieve this, we incorporate an optical cavity into this piezo-Brillouin system.

3. FULLY RESONANTLY ENHANCED PIEZO-BRILLOUIN SPECTROSCOPY

Including an optical cavity in this piezo-Brillouin system allows for resonant enhancements of both the optical pump and signal fields [44]. As demonstrated in prior works [17,19], a Fabry-Perot

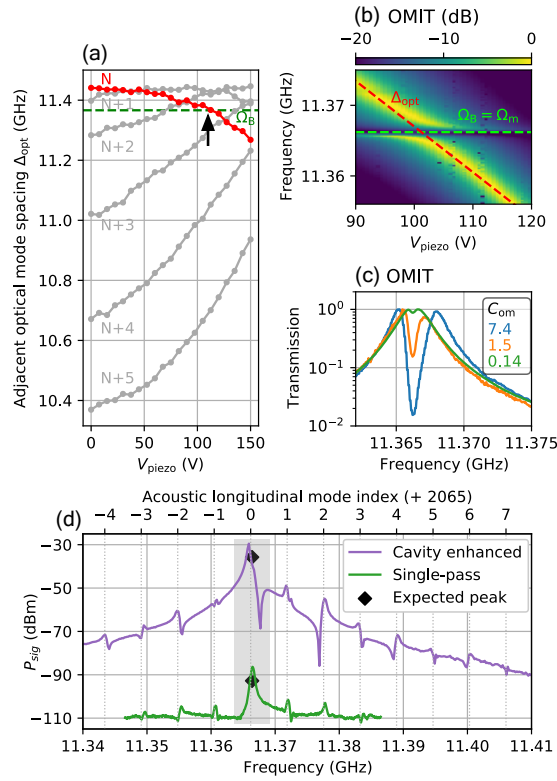


Fig. 2. Enhancing piezo-Brillouin spectroscopy using resonant optomechanical interactions. (a) Optical mode spacing tunability. For λ_{opt} from 1545.8–1546.3 nm, we find six mode pairs (labeled by lower longitudinal mode index N through $N + 5$) with spacings from 10.4 GHz to 11.5 GHz. By increasing V_{piezo} (thus changing cavity length), individual mode spacings can be varied by up to 500 MHz, allowing one mode pair (red) to be matched to the Ω_B (green dashed line) (b) Normalized OMIT spectra, as Δ_{opt} is tuned through Ω_B , using the piezo actuator. When $\Delta_{\text{opt}} = \Omega_B$, an anti-crossing is observed, with a splitting that exceeds the cavity linewidth, indicating the onset of strong coupling. (c) Single OMIT spectra at $\Delta_{\text{opt}} = \Omega_B$ with fitted cooperativities ranging from $C_{\text{om}} = 7.4 \sim 0.14$. (d) Single-pass and cavity-enhanced piezo-Brillouin spectroscopy. Sideband power at the swept microwave drive frequency is measured via heterodyne with the pump (1 kHz resolution bandwidth). Gray box indicates the main phonon mode of interest, with theoretically predicted peak amplitude shown as black dots. Other acoustic modes are spaced by the expected FSR (≈ 5.5 MHz) and have couplings consistent with mode and phase matching. To facilitate comparison more easily, the green data have been shifted down in frequency by nine FSRs to compensate for a $\sim 0.5\%$ shift of microwave resonance frequency between cooldowns.

cavity is well suited to this task, with Gaussian modes that achieve good spacial overlap with highly confined HBAR modes [see Figs. 1(a) and 1(b)]. Compared to the single-pass interaction, the effect of this optical resonator is to increase the optomechanical cooperativity (and thus P_{sig}) by a factor of \mathcal{F}^2 , where \mathcal{F} is the cavity finesse, a quantity that indicates the number of round trips before decay (see Supplement 1). Specifically, the cavity optomechanical cooperativity is now $C_{\text{om}} = \frac{4g_{\text{om}}^2}{\kappa_{\text{opt}}\Gamma}$, with $g_{\text{om}} = \sqrt{N_{\text{cav}}}g_{\text{om},0}$, where N_{cav} is now the intracavity photon number, and κ_{opt} is the optical cavity dissipation rate. Note that, compared to the single-pass coupling rate, $g_{\text{om},0}$ acquires a factor of $\frac{L_m}{L_{\text{opt}}}$, corresponding to a geometric filling factor between the acoustic and optical cavities.

For our optical cavity geometry, even a modest finesse ($\mathcal{F} > 1000$) results in optical linewidths that are orders of magnitude less than the mechanical frequency (i.e., $\kappa/\Omega_m \sim 10^{-3}$). In this deeply resolved sideband regime, it becomes necessary to use separate resonances to enhance the pump and signal, thus imposing an additional requirement that the optical mode spacing closely matches the acoustic frequency ($\Delta_{\text{opt}} \equiv \omega_{\text{opt}} - \omega_p = \Omega_m$).

Two features of this hybrid system allow us to meet this requirement. First, the Fresnel reflections at the vacuum–dielectric interface produced by the HBAR cause the optical mode spacing to be wavelength dependent. For instance, in our hybrid quartz cavity, over a ~ 1 nm range in pump wavelength, we find nine optical modes with spacings varying from 10.4 GHz to 11.5 GHz, which allows us to identify several pairs of modes with a frequency spacing that approximately matches Ω_B . Note that this variable FSR allows selective enhancement of either the Stokes or anti-Stokes process. While this coarse frequency matching was possible in prior works [17,19], here, we incorporate a piezo actuator (voltage, V_{piezo}) onto one of the mirrors, to enable more precise control required in this multiply resonant system. This allows the cavity length to be varied by approximately 500 nm, which can yield >100 MHz tunability in the optical mode spacing [see Fig. 2(a)].

This matching of the optical mode spacing to the mechanical frequency enables strong optomechanical interactions, which we illustrate in Figs. 2(b) and 2(c). We lock a laser to the lower frequency (pump) mode, and sweep a sideband over the higher frequency (signal) mode. When $\Delta_{\text{opt}} \neq \Omega_m$, this swept probe simply shows the optical response of the signal mode. Applying a voltage to the piezo actuator, we can smoothly vary the optical mode spacing from 11.355 GHz to 11.375 GHz [red dashed line in Fig. 2(b)], revealing an avoided crossing when $\Delta_{\text{opt}} = \Omega_m$. This phenomenon is known as optomechanically induced transparency (OMIT), and is the result of optical interference with a photoelastically driven motional sideband [46]. OMIT measurements offer a convenient tool for characterizing the strength of our optomechanical interaction. Specifically, the depth and width of the OMIT feature offer direct measurement of the optomechanical cooperativity, with minimal assumptions. Figure 2(c) shows OMIT spectra for various pump powers. The extracted cooperativities scale linearly with intracavity power, as expected, reaching $C_{\text{om}} = 7$ ($g_{\text{om}} = 1.4$ MHz) at a pump power of 110 mW. Combining this g_{om} with the estimated intra-cavity photon number, we can obtain an experimental value for single-photon optomechanical coupling rate, $g_{\text{om},0} = 5.28$ Hz, close to the theoretical value, $g_{\text{om},0} = 5.89$ Hz. Figures 2(b) and 2(c) also illustrate that this system approaches the optomechanical strong coupling regime ($2g_{\text{om}} > \kappa_{\text{opt}}, \Gamma$), visible as the emergence of normal-mode splitting [19]. Such strong coupling can be of value in hybrid quantum systems for rapid manipulation of intracavity states.

With this doubly resonant optical enhancement established, we repeat the measurement from Fig. 2(d), wherein a microwave drive piezoelectrically generates phonons, and we measure the optical sideband scattered off a strong pump. The transmitted optical signal is collected from the cavity and measured via a heterodyne beat note with the pump. The optical response from the microwave drive ($P_{\mu} = 1$ mW) is shown in purple in Fig. 2(d). The central phase-matched acoustic mode ($\Omega_m/2\pi = 11.366$ GHz) is indicated by a gray shaded box. Comparing the cavity-enhanced and single-pass spectra, we observe a ~ 60 dB increase in scattered optical power, consistent with the predicted \mathcal{F}^2 enhancement in cooperativity (for details, see Supplement 1).

The cavity-enhanced data illustrate several prominent features that are consistent with the underlying coupling mechanisms. On the tails of the central, phase-matched peak ($\Omega_m/2\pi = 11.366$ GHz), we see the other longitudinal modes, whose motion coherently interferes to yield Fano line shapes. The apparent coupling rates of these modes are suppressed according to the optical phase-matching condition ($\text{sinc}^2[(\Omega - \Omega_B)/4\Delta_m]$), as well as the piezoelectric mode overlap (which suppresses coupling to even-index modes). Away from the central mode, the piezo-Brillouin spectrum is further suppressed by the optical and microwave cavity susceptibilities. There is also a significant Fano dip associated with the main peak at $\Omega_m/2\pi = 11.366$ GHz. This is a result of a residual Pockels-type electro-optic (EO) coupling in quartz [47], which destructively interferes with the piezo-optomechanical signal. This Fano shape results in a slightly higher response on the left side of the peak. The relative contribution of the EO effect to the piezo-Brillouin interaction can be reduced by increasing g_{em} or decreasing Γ . Alternatively, this effect could be intentionally amplified in a device focused on EO interactions.

4. TRANSDUCTION

The measurements in Fig. 2 establish that this system achieves simultaneous, fully resonant electro- and optomechanical couplings (with $C_{\text{om}} > 1$). This motivates us to evaluate the performance of this platform from the perspective of quantum transduction, quantifying the efficiency with which it converts microwave photons to optical photons. In our system, the transduction efficiency η [defined as the scattered optical photons exiting the Fabry-Perot cavity per microwave photon entering through the coupling pin; see Fig. 1(a)] can be analytically expressed in terms of the electro/opto-mechanical cooperativities as [23,28]

$$\eta = \eta_{\text{opt}}\eta_{\mu} \frac{4C_{\text{om}}C_{\text{em}}}{(1 + C_{\text{om}} + C_{\text{em}})^2}. \quad (3)$$

Here, η_{opt} and η_{μ} are the optical and microwave port-coupling efficiencies (i.e., the fraction of the total loss rate attributable to the input/output port). Thus, one seeks to have greater-than-unity (and equal) cooperativities for both subsystems, as well as efficiently coupled ports for transferring photons in and out. In the hybrid quartz cavity demonstrated in Fig. 2, we reach coupling efficiencies of $\eta_{\mu} = 0.43$ and $\eta_{\text{opt}} = 0.53$. Higher coupling efficiencies (i.e., over-coupled resonators) are possible by adjusting the microwave coupling pin and using optical mirrors with imbalanced reflectivities. We note that the modes of Gaussian optical resonators easily achieve high fiber-coupling efficiency, which is a key challenge for low-loss integration.

Repeating the measurements of Fig. 2(d), we can characterize the microwave-to-optical scattering parameter and extract η_{oe} (optical photons out per microwave photon in). Alternatively, we can inject a sideband into the optical signal mode, and directly measure the microwave response, to characterize η_{eo} (microwave photons out per optical photon in). Both measurements are shown in Fig. 3(a), illustrating the bidirectionality of this device. The Fano dip in the η_{oe} data results from the previously described EO transduction. The added noise floor of this transduction would be set by the thermal noise of the acoustic resonator, with an expected 16 phonons at 9 K temperature. Characterization of the thermal

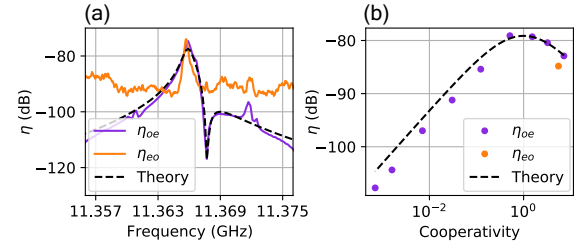


Fig. 3. Bidirectional electro-opto-mechanical transduction. (a) Transduction spectra for both microwave-to-optical (η_{oe} , purple, $C_{\text{om}} = 1.53$) and optical-to-microwave (η_{eo} , orange, $C_{\text{om}} = 5.50$). Dashed black line is theoretical prediction of the transduction spectra. The elevated noise floor in η_{eo} is set by room-temperature amplifiers/detectors. (b) Transduction efficiency at phonon frequency ($\Omega_m/2\pi = 11.3663$ GHz) in relation to optomechanical cooperativity controlled via optical pump power. Purple dots are the microwave-to-optical data. Orange dot is an optical-to-microwave measurement. Both data are expected to follow the black dashed theory line.

noise in this quartz system was not carried out, but similar measurements on CaF_2 confirm good thermalization (see Section 5), consistent with past works [19]. The higher noise floor in the η_{eo} data is a combination of Johnson noise of the room-temperature microwave detector, microwave amplifier noise, and detector noise.

On resonance, ($\Omega_m/2\pi = 11.366$ GHz), we verify that the transduction efficiency scales as predicted with optical cooperativity. The experimental data (purple points) in Fig. 3(b) well describe the theoretical curve (black dashed line) following Eq. (3), assuming $C_{\text{em}} = 5.6 \times 10^{-8}$. In particular, we confirm that the transduction is maximized for $C_{\text{om}} = 1$, implying that our optomechanical subsystem is sufficiently strongly coupled to saturate the transduction efficiency. Further increased C_{om} damps the acoustic resonance, reducing the overall efficiency. Note that the model is well matched to the data for $g_{\text{em}}/2\pi = 347$ Hz ($C_{\text{em}} = 5.6 \times 10^{-8}$), instead of the simulated $g_{\text{em}}/2\pi = 298$ Hz ($C_{\text{em}} = 4.18 \times 10^{-8}$). This may be attributable to a discrepancy between the simulated microwave resonator and the assembled device.

The data presented in Fig. 3 illustrate the current performance of this device, where we observe a maximum conversion of $\eta = 1.2^{+1.0}_{-0.6} \times 10^{-8}$, with a bandwidth of 500 kHz. The uncertainty here comes from detector and cable loss calibrations. With coupling efficiencies exceeding 10^{-1} and optomechanical cooperativity exceeding one, the performance is currently limited by low electromechanical cooperativity. However, our ability to reach $C_{\text{om}} = 1$ indicates that we are maximally sensitive to forces acting on the resonator. This motivates the possibility of using our platform as a sensitive phonon spectroscopy tool, with applications in materials science.

5. PRECISION SENSING OF ANOMALOUS PIEZOELECTRICITY

This sensitivity, combined with the modular construction of the system, makes it possible to investigate electromechanical couplings in a variety of materials. In particular, it enables us to probe possible anomalous piezoelectricity in non-piezoelectric materials. There is strong motivation for this type of study, as parasitic piezoelectricity may be a relevant loss channel for emerging solid state quantum technologies [48–50]. Subsurface lattice damage, or even

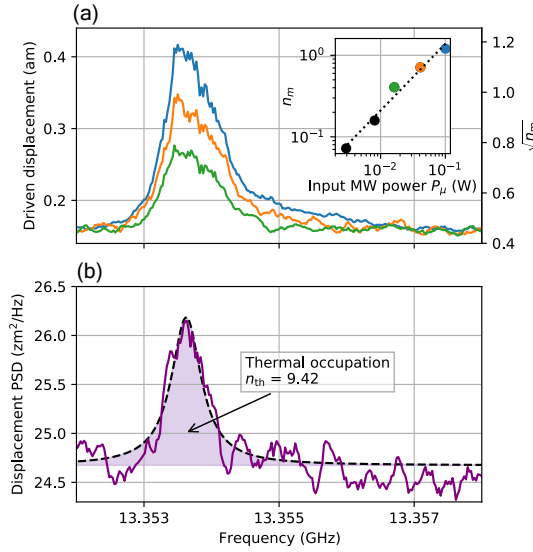


Fig. 4. Spectroscopy of anomalous piezoelectricity in CaF_2 . (a) Coherent, cavity-enhanced optical spectroscopy of microwave-driven motion in CaF_2 . The amplitude of driven motion (characterized by $\sqrt{n_m}$, where n_m is phonon number) is calculated from the detected optical signal. The inset shows the linear relation (black dashed line) between the peak driven motion (in units of phonon number) and microwave power. To obtain the driven motion, background noise from the main figure is subtracted in the inset data. The color of each datapoint matches that of the main graph. Black points are not plotted in the main graph. (b) Amplitude spectral density of undriven (thermal) motion. PSD, power spectral density. Black dashed line is a Lorentzian fit with 535 kHz linewidth. Shaded area under the Lorentzian fit is integrated to obtain the effective mechanical occupation of $n_{th} = 9.42$. The peak of the Lorentzian fit indicates detection sensitivity, corresponding to $2.1 \times 10^{-4} \text{ phonons} \cdot \text{Hz}^{-1}$.

the inherent asymmetry of the lattice boundary [39], can disrupt the centro-symmetry of nominally non-piezoelectric materials.

One such material not expected to have a piezoelectric response is CaF_2 . The Brillouin-active mechanical frequency for CaF_2 is ~ 13.3 GHz, which we can easily target by adjusting the microwave resonator and optical FSR. Doing so, we can repeat the experiment from Fig. 2(d), applying a microwave drive at the CaF_2 Brillouin frequency and looking for an optical response. The results of this experiment are shown in Fig. 4(a), where we clearly see non-zero microwave-driven motion, indicating a measurable electro-mechanical coupling (see Supplement 1 for experimental parameters). The detected signal exists only at the Brillouin frequency, indicating that it is indeed a mechanical response. This rules out the possibility that the response is originating from an unexpected electro-optical coupling. As shown in the inset of Fig. 4(a), we observe a linear electromechanical coupling. We refer to this coupling as anomalous piezoelectricity, although the innate mechanisms of such an effect are uncertain (e.g., charged surfaces and crystal defects). Subtracting background noise (consisting of shot noise and detector noise) and thermal noise from the response shown in Fig. 4(a), we detect a coherent acoustic response corresponding to $n_m = 1.2$, or a peak displacement for our acoustic standing wave of 0.25 am. This corresponds to an effective electromechanical coupling rate of $g_{em}^{\text{CaF}_2}/2\pi = 0.03$ Hz.

This effective piezoelectricity could be attributed to imperfections distributed in the bulk or concentrated at the surface. If the acoustic response was derived from a piezoelectric coupling across

a thin surface layer of 1 nm [39,48], it would correspond to an effective piezoelectric constant of $d_{33} = 2.44$ pm/V (comparable to common piezoelectric materials). However, such a large piezoelectric coefficient would be inconsistent with other investigations into CaF_2 [38], and quantitative interferometric-based piezo force microscopy (IDS-PFM) [51,52] measurements conducted on this sample (which revealed no signal; see Supplement 1). Alternatively, if it is derived from a uniform piezoelectric coupling distributed through the bulk of the crystal [36–38], it would correspond to a weak effective d_{33} of 0.083 fm/V, which would be consistent with the previously mentioned null results from IDS-PFM (given measurement noise floor of 55 fm/V). To explain this effective bulk property, one might consider an ensemble of polar defects, which effectively act as piezoelectric emitters. Such a mechanism could be intrinsically linked to dielectric loss, motivating further study, particularly in the context of solid state qubit decoherence.

As in transduction, the fundamental noise floor of this technique is ultimately limited by the thermal noise of the acoustic resonator, which we can detect in the absence of the microwave drive [see Fig. 4(b)]. The effective thermal motion we detect corresponds to an average occupation of $n_{th} = 9.42$ (at $C_{om} = 0.4$), consistent with thermalization to the cryostat ($T = 8.7$ K) plus some laser cooling by the pump. Note that we observe no significant heating despite > 100 mW of input pump power, highlighting the good thermal anchoring and minimal absorption in this bulk platform. On resonance, this thermal-limited noise floor is 162 zm (0.21 phonons) in the 1 kHz bandwidth of our driven measurement, which corresponds to a piezoelectric coefficient sensitivity of 7 am/V, or 2.2 am/V at a bandwidth of 100 Hz in the case of an evenly distributed bulk piezoelectricity. This compares favorably to existing techniques for probing piezoelectricity, such as resonant piezoelectric spectroscopy (RPS), resonant ultrasound spectroscopy (RUS) [38], and PFM [51,52]. Critically, our technique extends this sensitivity to GHz frequencies and cryogenic temperatures. Applying this new materials analysis tool to materials such as silicon, sapphire, and diamond can be of immediate relevance to quantum technologies [39,40,48–50].

6. OUTLOOK AND CONCLUSION

Much progress has been made in both EO and piezo-opto-mechanical transduction in recent years, reaching $\eta \sim \mathcal{O}(10^{-1})$ with minimal added noise [29,53] and achieving preliminary integration with superconducting qubits [29,54]. However, given the qualitative advantages of this platform, including robust thermal properties and power handling, high optical collection efficiency, and modularity, it is interesting to consider the outlook for efficient transduction.

Since C_{om} , η_{opt} , and η_{μ} are of order unity, future transduction improvements must target C_{em} . First, since $C_{em} \propto g_{em}^2 \propto d_{33}^2$, a stronger piezoelectric such as LiNbO_3 or BaTiO_3 can immediately improve η (e.g., by $50\times$ for LiNbO_3). Recalling that this platform requires no nanofabrication on the sample, it is straightforward to make such material changes. There is also room for further optimization of mode matching between the acoustic and microwave resonators. For example, a larger acoustic waist could increase C_{em} by $80\times$, and a re-entrant microwave cavity (with increased field concentration) could increase C_{em} by $\sim 10\times$. Other extensions based on planar microwave resonators or piezoelectric superlattices may offer additional gains in electromechanical coupling, and merit further investigation.

Table 1. System Modifications to Improve C_{em} , Contributing to Both Transduction Efficiency and Piezo-Detection Sensitivity

	C_{em}
Current experiment	5.6×10^{-8}
Stronger piezoelectric material	$\uparrow 50\times$
Acoustic mode optimization	$\uparrow 80\times$
Microwave mode optimization	$\uparrow 10\times$
Higher microwave cavity-Q	$\uparrow 10^2\times$
Higher acoustic cavity-Q	$\uparrow 10^3\times$
Combined improvements	$\uparrow \sim 10^9\times$

There is also significant room to improve the lifetimes of the component microwave and acoustic resonators, increasing electro-mechanical cooperativity. For instance, this demonstration uses a non-superconducting copper microwave cavity, with a modest $Q < 1000$. Moving to a superconducting metal, there is ample evidence for both post and re-entrant cavities with $Q > 10^7$ [42]. While co-integrating superconducting resonators with optics is a known technical challenge [29], this macroscopic, 3D platform may offer increased robustness of the superconducting resonator [31]. Additionally, while current acoustic performance is limited by diffraction loss, newly developed fabrication techniques allow us to produce stable plano-convex resonators with $Q > 10^7$ [41]. Implementation of acoustic resonators with better Q also allows us to reach $C_{om} > 1$ with weaker pump power (e.g., with $Q_m = 10^7$, $C_{om} = 1$ requires only $P_p \approx 1 \mu W$), increasing compatibility with mK cryogenic systems.

Together, these improvements highlight a feasible path from the $\eta = 1.2 \times 10^{-8}$ demonstrated here towards bidirectional transduction with near unity efficiency. Within the landscape of transduction platforms, piezo-Brillouin systems such as this have a unique set of advantages and constraints, and merit further investigation for quantum applications.

Beyond transduction, we have demonstrated how this system presents a versatile platform for materials analysis and other technological pursuits. Specifically, Brillouin optical readout offers the ability to conduct precision spectroscopy of GHz motion with single-quantum sensitivity (i.e., a noise floor of $5.12 \text{ zm} \cdot \text{Hz}^{-1/2}$). We have demonstrated how this can be used to investigate parasitic piezoelectricity, with detectable electromechanical coupling as low as $g_{em}^{CaF_2}/2\pi = 0.03 \text{ Hz}$. Note that most of the improvements in Table 1 would also benefit such spectroscopy efforts, with the possibility of detecting parasitic couplings that are many orders of magnitude smaller. Such measurements open the door to further evaluation of substrate purity and surface treatments, of critical importance in quantum technologies. The dual microwave/optical functionality may also be useful for investigating strain-active solid state defects. Specifically, the resonant piezoelectric drive presents a mechanism for rapidly actuating strain fields, and the optical cavity offers the possibility of Purcell-enhanced photon collection.

Funding. U.S. Department of Energy (DE-SC0012704, DE-SC0019406).

Acknowledgment. We thank F. Ruesink, Y. Luo, S. Gertler, S. Ganjam, A. Read, N. Jin, Y. Zhou, M. Pavlovich, H. Cheng, and Y. Dahmani for helpful discussions. Facilities use was supported by Yale SEAS cleanroom, Yale West Campus cleanroom, and Yale Gibbs machine shop. This research was initially supported by the U.S. Department of Energy, Office of Science, and completed under support by the U.S. Department of Energy, Office of Science, National Quantum Information Science Research Centers, and Co-design Center for Quantum Advantage (C2QA). Piezoresponse force microscopy research was

supported by the Center for Nanophase Materials Sciences (CNMS), which is a U.S. Department of Energy, Office of Science User Facility at Oak Ridge National Laboratory. This paper has been authored by UT-Battelle, LLC with the U.S. Department of Energy.

Disclosures. The authors declare no conflicts of interest.

Data availability. Data underlying the results presented in this paper are not publicly available at this time but may be obtained from the authors upon reasonable request.

Supplemental document. See Supplement 1 for supporting content.

[†]These authors contributed equally to this work.

REFERENCES

1. G. Kurizki, P. Bertet, Y. Kubo, K. Mølmer, D. Petrosyan, P. Rabl, and J. Schmiedmayer, "Quantum technologies with hybrid systems," *Proc. Natl. Acad. Sci. USA* **112**, 3866–3873 (2015).
2. J. Chan, T. P. M. Alegre, A. H. Safavi-Naeini, J. T. Hill, A. Krause, S. Gröblacher, M. Aspelmeyer, and O. Painter, "Laser cooling of a nanomechanical oscillator into its quantum ground state," *Nature* **478**, 89–92 (2011).
3. A. D. O'Connell, M. Hofheinz, M. Ansmann, R. C. Bialczak, M. Lenander, E. Lucero, M. Neeley, D. Sank, H. Wang, M. Weides, J. Wenner, J. M. Martinis, and A. N. Cleland, "Quantum ground state and single-phonon control of a mechanical resonator," *Nature* **464**, 697–703 (2010).
4. E. Verhagen, S. Deléglise, S. Weis, A. Schliesser, and T. J. Kippenberg, "Quantum-coherent coupling of a mechanical oscillator to an optical cavity mode," *Nature* **482**, 63–67 (2012).
5. J. D. Teufel, T. Donner, D. Li, J. W. Harlow, M. S. Allman, K. Cicak, A. J. Sirois, J. D. Whittaker, K. W. Lehnert, and R. W. Simmonds, "Sideband cooling of micromechanical motion to the quantum ground state," *Nature* **475**, 359–363 (2011).
6. S. Maity, L. Shao, S. Bogdanović, S. Meesala, Y.-I. Sohn, N. Sinclair, B. Pingault, M. Chalupnik, C. Chia, L. Zheng, K. Lai, and M. Lončar, "Coherent acoustic control of a single silicon vacancy spin in diamond," *Nat. Commun.* **11**, 193 (2020).
7. S. J. Whiteley, G. Wolfowicz, C. P. Anderson, A. Bourassa, H. Ma, M. Ye, G. Koolstra, K. J. Satzinger, M. V. Holt, F. J. Heremans, A. N. Cleland, D. I. Schuster, G. Galli, and D. D. Awschalom, "Spin-phonon interactions in silicon carbide addressed by Gaussian acoustics," *Nat. Phys.* **15**, 490–495 (2019).
8. Y. Chu, P. Kharel, W. H. Renninger, L. D. Burkhardt, L. Frunzio, P. T. Rakich, and R. J. Schoelkopf, "Quantum acoustics with superconducting qubits," *Science* **358**, 199–202 (2017).
9. A. Beccari, D. A. Visani, S. A. Fedorov, M. J. Beryhi, V. Boureau, N. J. Engelsens, and T. J. Kippenberg, "Strained crystalline nanomechanical resonators with quality factors above 10 billion," *Nat. Phys.* **18**, 436–441 (2022).
10. G. S. MacCabe, H. Ren, J. Luo, J. D. Cohen, H. Zhou, A. Sipahigil, M. Mirhosseini, and O. Painter, "Nano-acoustic resonator with ultralong phonon lifetime," *Science* **370**, 840–843 (2020).
11. S. Gallioui, M. Goryachev, R. Bourquin, P. Abbé, J. P. Aubry, and M. E. Tobar, "Extremely low loss phonon-trapping cryogenic acoustic cavities for future physical experiments," *Sci. Rep.* **3**, 2132 (2013).
12. W. Liekens, L. Michiels, and A. D. Bock, "On the attenuation of 9.4 GHz longitudinal hypersonic waves in some trigonal crystals," *J. Phys. C* **4**, 1124–1129 (1971).
13. J. Thaxter and P. Tannenwald, "Phonon generation, propagation, and attenuation at 70 GHz," *IEEE Trans. Sonics Ultrasonics* **13**, 61–68 (1966).
14. R. Y. Chiao, C. H. Townes, and B. P. Stoicheff, "Stimulated Brillouin scattering and coherent generation of intense hypersonic waves," *Phys. Rev. Lett.* **12**, 592–595 (1964).
15. W. H. Renninger, P. Kharel, R. O. Behunin, and P. T. Rakich, "Bulk crystalline optomechanics," *Nat. Phys.* **14**, 601–607 (2018).
16. J. Bourhill, N. C. Carvalho, M. Goryachev, S. Gallioui, and M. E. Tobar, "Generation of coherent phonons via a cavity enhanced photonic lambda scheme," *Appl. Phys. Lett.* **117**, 164001 (2020).
17. P. Kharel, G. I. Harris, E. A. Kittlaus, W. H. Renninger, N. T. Otterstrom, J. G. E. Harris, and P. T. Rakich, "High-frequency cavity optomechanics using bulk acoustic phonons," *Sci. Adv.* **5**, eaav0582 (2019).

18. Y. Chu, P. Kharel, T. Yoon, L. Frunzio, P. T. Rakich, and R. J. Schoelkopf, "Creation and control of multi-phonon Fock states in a bulk acoustic-wave resonator," *Nature* **563**, 666–670 (2018).
19. P. Kharel, Y. Chu, E. A. Kittlaus, N. T. Otterstrom, S. Gertler, and P. T. Rakich, "Multimode strong coupling in cavity optomechanics," *Phys. Rev. Appl.* (to be published).
20. E. Zeuthen, A. Schliesser, A. S. Sørensen, and J. M. Taylor, "Figures of merit for quantum transducers," *Quantum Sci. Technol.* **5**, 034009 (2020).
21. N. Lauk, N. Sinclair, S. Barzanjeh, J. P. Covey, M. Saffman, M. Spiropulu, and C. Simon, "Perspectives on quantum transduction," *Quantum Sci. Technol.* **5**, 020501 (2020).
22. Y. Chu and S. Gröblacher, "A perspective on hybrid quantum opto- and electromechanical systems," *Appl. Phys. Lett.* **117**, 150503 (2020).
23. R. W. Andrews, R. W. Peterson, T. P. Purdy, K. Cicak, R. W. Simmonds, C. A. Regal, and K. W. Lehnert, "Bidirectional and efficient conversion between microwave and optical light," *Nat. Phys.* **10**, 321–326 (2014).
24. A. Vainsencher, K. J. Satzinger, G. A. Peairs, and A. N. Cleland, "Bidirectional conversion between microwave and optical frequencies in a piezoelectric optomechanical device," *Appl. Phys. Lett.* **109**, 033107 (2016).
25. K. C. Balram, M. I. Davanço, J. D. Song, and K. Srinivasan, "Coherent coupling between radiofrequency, optical and acoustic waves in piezo-optomechanical circuits," *Nat. Photonics* **10**, 346–352 (2016).
26. W. Jiang, C. J. Sarabalis, Y. D. Dahmani, R. N. Patel, F. M. Mayor, T. P. McKenna, R. Van Laer, and A. H. Safavi-Naeini, "Efficient bidirectional piezo-optomechanical transduction between microwave and optical frequency," *Nat. Commun.* **11**, 1166 (2020).
27. M. Forsch, R. Stockill, A. Wallucks, I. Marinković, C. Gärtner, R. A. Norte, F. van Otten, A. Fiore, K. Srinivasan, and S. Gröblacher, "Microwave-to-optics conversion using a mechanical oscillator in its quantum ground state," *Nat. Phys.* **16**, 69–74 (2020).
28. X. Han, W. Fu, C. Zhong, C.-L. Zou, Y. Xu, A. A. Sayem, M. Xu, S. Wang, R. Cheng, L. Jiang, and H. X. Tang, "Cavity piezo-mechanics for superconducting-nanophotonic quantum interface," *Nat. Commun.* **11**, 3237 (2020).
29. M. Mirhosseini, A. Sipahigil, M. Kalaei, and O. Painter, "Superconducting qubit to optical photon transduction," *Nature* **588**, 599–603 (2020).
30. A. Rueda, F. Sedlmeir, M. C. Collodo, U. Vogl, B. Stiller, G. Schunk, D. V. Strekalov, C. Marquardt, J. M. Fink, O. Painter, G. Leuchs, and H. G. L. Schwefel, "Efficient microwave to optical photon conversion: an electro-optical realization," *Optica* **3**, 597–604 (2016).
31. W. Hease, A. Rueda, R. Sahu, M. Wulf, G. Arnold, H. G. Schwefel, and J. M. Fink, "Bidirectional electro-optic wavelength conversion in the quantum ground state," *PRX Quantum* **1**, 020315 (2020).
32. J. Holzgrafe, N. Sinclair, N. Sinclair, D. Zhu, D. Zhu, A. Shams-Ansari, M. Colangelo, Y. Hu, Y. Hu, M. Zhang, M. Zhang, K. K. Berggren, and M. Lončar, "Cavity electro-optics in thin-film lithium niobate for efficient microwave-to-optical transduction," *Optica* **7**, 1714–1720 (2020).
33. L. Shao, M. Yu, S. Maity, N. Sinclair, L. Zheng, C. Chia, A. Shams-Ansari, C. Wang, M. Zhang, K. Lai, and M. Lončar, "Microwave-to-optical conversion using lithium niobate thin-film acoustic resonators," *Optica* **6**, 1498–1505 (2019).
34. L. Fan, C.-L. Zou, R. Cheng, X. Guo, X. Han, Z. Gong, S. Wang, and H. X. Tang, "Superconducting cavity electro-optics: a platform for coherent photon conversion between superconducting and photonic circuits," *Sci. Adv.* **4**, eaar4994 (2018).
35. T. Blésin, H. Tian, S. A. Bhave, and T. J. Kippenberg, "Quantum coherent microwave-optical transduction using high-overtone bulk acoustic resonances," *Phys. Rev. A* **104**, 052601 (2021).
36. W. H. Robinson, A. J. Glover, and A. Wolfenden, "Electrical-mechanical coupling of dislocations in KCl, NaCl, LiF, and CaF₂," *Phys. Status Solidi A* **48**, 155–163 (1978).
37. N. D. Sharma, R. Maranganti, and P. Sharma, "On the possibility of piezoelectric nanocomposites without using piezoelectric materials," *J. Mech. Phys. Solids* **55**, 2328–2350 (2007).
38. O. Aktas, M. Kangama, G. Linyu, G. Catalan, X. Ding, A. Zunger, and E. K. H. Salje, "Piezoelectricity in nominally centrosymmetric phases," *Phys. Rev. Res.* **3**, 043221 (2021).
39. A. B. Georgescu and S. Ismail-Beigi, "Surface piezoelectricity of (0001) sapphire," *Phys. Rev. Appl.* **11**, 064065 (2019).
40. J. R. Maze, A. Gali, E. Togan, Y. Chu, A. Trifonov, E. Kaxiras, and M. D. Lukin, "Properties of nitrogen-vacancy centers in diamond: the group theoretic approach," *New J. Phys.* **13**, 025025 (2011).
41. P. Kharel, Y. Chu, M. Power, W. H. Renninger, R. J. Schoelkopf, and P. T. Rakich, "Ultra-high-Q phononic resonators on-chip at cryogenic temperatures," *APL Photon.* **3**, 066101 (2018).
42. M. Reagor, W. Pfaff, C. Axline, R. W. Heeres, N. Ofek, K. Sliwa, E. Holland, C. Wang, J. Blumoff, K. Chou, M. J. Hatridge, L. Frunzio, M. H. Devoret, L. Jiang, and R. J. Schoelkopf, "Quantum memory with millisecond coherence in circuit QED," *Phys. Rev. B* **94**, 014506 (2016).
43. R. Tarumi, K. Nakamura, H. Ogi, and M. Hirao, "Complete set of elastic and piezoelectric coefficients of α -quartz at low temperatures," *J. Appl. Phys.* **102**, 113508 (2007).
44. R. Van Laer, R. Baets, and D. Van Thourhout, "Unifying Brillouin scattering and cavity optomechanics," *Phys. Rev. A* **93**, 053828 (2016).
45. M. Aspelmeyer, T. J. Kippenberg, and F. Marquardt, "Cavity optomechanics," *Rev. Mod. Phys.* **86**, 1391–1452 (2014).
46. S. Weis, R. Rivière, S. Deléglise, E. Gavartin, O. Arcizet, A. Schliesser, and T. J. Kippenberg, "Optomechanically induced transparency," *Science* **330**, 1520–1523 (2010).
47. V. Ivanov, "Direct electro-optic effect in langasites and α -quartz," *Opt. Mater.* **79**, 1–7 (2018).
48. L. B. Ioffe, V. B. Geshkenbein, C. Helm, and G. Blatter, "Decoherence in superconducting quantum bits by phonon radiation," *Phys. Rev. Lett.* **93**, 057001 (2004).
49. M. Scigliuzzo, L. E. Bruhat, A. Bengtsson, J. J. Burnett, A. F. Roudsari, and P. Delsing, "Phononic loss in superconducting resonators on piezoelectric substrates," *New J. Phys.* **22**, 053027 (2020).
50. I. Diniz and R. de Sousa, "Intrinsic photon loss at the interface of superconducting devices," *Phys. Rev. Lett.* **125**, 147702 (2020).
51. A. Labuda and R. Proksch, "Quantitative measurements of electro-mechanical response with a combined optical beam and interferometric atomic force microscope," *Appl. Phys. Lett.* **106**, 253103 (2015).
52. L. Collins, Y. Liu, O. S. Ovchinnikova, and R. Proksch, "Quantitative electromechanical atomic force microscopy," *ACS Nano* **13**, 8055–8066 (2019).
53. R. Sahu, W. Hease, A. Rueda, G. Arnold, L. Qiu, and J. M. Fink, "Quantum-enabled operation of a microwave-optical interface," *Nat. Commun.* **13**, 1276 (2022).
54. R. D. Delaney, M. D. Urmey, S. Mittal, B. M. Brubaker, J. M. Kindem, P. S. Burns, C. A. Regal, and K. W. Lehnert, "Superconducting-qubit readout via low-backaction electro-optic transduction," *Nature* **606**, 489–493 (2022).